Applied Geochemistry 183 (2025) 106332

Contents lists available at ScienceDirect

Applied Geochemistry

journal homepage: www.elsevier.com/locate/apgeochem

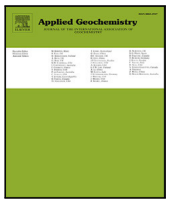

Investigation of plutonium diffusion profiles in Opalinus Clay rock via TOF-SIMS and rL-SNMS

Felix Berg *, Christopher Sirleaf, Janik Lohmann, Markus Breckheimer, Tobias Reich *

Johannes Gutenberg-Universität Mainz, Department of Chemistry - Nuclear Chemistry, 55099, Mainz, Germany

ARTICLE INFO

Editor - Xavier Gaona

Keywords:
Nuclear waste
Plutonium
Diffusion
Opalinus Clay
Resonant laser ionization
TOF-SIMS
rL-SNMS
CE-ICP-MS

ABSTRACT

The capability of the combined approach of time-of-flight secondary ion mass spectrometry (TOF-SIMS) and resonant laser secondary neutral mass spectrometry (rL-SNMS) for the analysis of diffusion samples of ^{242}Pu in Opalinus Clay (OPA) under aerobic conditions was investigated at the micrometer scale. The speciation of Pu in the diffusion reservoir with OPA pore water (pH 7.6) was determined as PuO_2^+ using capillary electrophoresis coupled to inductively coupled plasma mass spectrometry (CE-ICP-MS). Using modern 3D printing techniques, a simple and easily scalable experimental setup was developed and adapted to the requirements of TOF-SIMS and rL-SNMS. Together, these techniques allowed for the observation of the pristine diffusion profile of Pu while retaining information about the heterogeneous clay rock. For the experiment with 35 days of in-diffusion, the modeling of an averaged diffusion profile of approximately 300 µm length resulted in $D_a = 3.2(4) \times 10^{-15}$ m^2 s^{-1}. TOF-SIMS and rL-SNMS mappings showed heterogeneous distributions of Pu inside the clay rock and correlations with the matrix elements Fe and Ca, pointing to pyrite and a cementing calcite phase as reactive mineral phases.

1. Introduction

Due to the long half-life of its isotopes, their high radiotoxicity and vast aqueous chemistry with multiple oxidation states possibly present at the same time, the trans-uranium element plutonium (Pu) is of major interest for the safety case for nuclear waste storage of high-level radioactive waste (HLW) (Geckeis et al., 2019). Many countries with a current or former nuclear energy program plan for the safekeeping of HLW in a deep geological repository (DGR) using a multi-barrier concept with a combination of (geo-)technical and geological barriers. The latter is of particular significance since the man-made measures are not expected to last for the total storage time required for HLW of up to one million years (Bundesgesetzblatt, 2017). Since no experimental data for a potential construction site of a DGR under investigation can be obtained over such a long period, the safety case then rests on models that are predicting the behaviour of the radioactive inventory and its interactions with the different barrier components using parameters retrieved in laboratory experiments. It is therefore vital to study the (geo-)chemical interactions of radionuclides as closely as possible and gain an in-depth knowledge about the underlying processes. Possible host-rock formations considered due to their unique favourable properties for a DGR are rock salt, crystalline and clay rocks. Many European countries are researching or already planning to build their DGR in clay rock (Preter, 2023; Andra, 2022; Nagra, 2022), for which, among others, Opalinus Clay (OPA) is a potential candidate. OPA and other clay rocks in general provide reducing conditions which are considered favourable for fission products and actinides such as Pu since their reduced species show less mobility (Churakov et al., 2020). However, still many questions remain concerning the stability of the reducing environment, the kinetics and the redox active components, i.e. the minerals (Maes et al., 2024). For this reason, the chemical interactions of various radionuclides and OPA have already been the subject of extensive research efforts in a wide variety of experiments (Wu et al., 2009; Joseph et al., 2013; Montavon et al., 2022). The insights and parameters retrieved for sorption and migration are usually averaged over the bulk material: for example, distribution coefficients are regularly obtained from batch sorption experiments with OPA suspensions. Samples from diffusion studies are often analyzed via abrasive peeling (Van Loon and Müller, 2014). Therefore, any information about the exact processes and various mineral phases possibly involved in the retention of a radionuclide, i.e. the microstructure, is lost. A spatially resolved approach would allow to gain further insight into the underlying processes.

Time-of-flight secondary-ion mass spectrometry (TOF-SIMS) is a technique for the spatially resolved analysis of surfaces at the micrometer or even nanometer scale: a pulsed primary ion (PI) beam is scanned

* Corresponding authors.
E-mail addresses: feberg@uni-mainz.de (F. Berg), treich@uni-mainz.de (T. Reich).

https://doi.org/10.1016/j.apgeochem.2025.106332
Received 29 October 2024; Received in revised form 21 February 2025; Accepted 22 February 2025
Available online 8 March 2025

over the sample, creating secondary ions (SIs) which are subsequently analyzed by their mass-to-charge ratio (m/z) in a TOF-MS. This way, a full mass spectrum is retrieved for every position sampled. By comparing the relative intensities of a mass peak for the various positions, the qualitative distribution of said mass on the sample's surface is mapped, which allows for conclusions about the surface's composition. One major drawback of TOF-SIMS is the possibility of isobaric interferences, especially if the concentration of analyte is as low as in the far-field of a DGR. Resonance ionization mass spectrometry (RIMS) is a highly sensitive and selective analytical technique that is able to address this shortcoming. Here, atomic species are photo-ionized via laser light in a multi-step excitation scheme, using the unique electronic structure of every element. Isotopes are then usually separated in a mass analyzer. Depending on the element and the excitation scheme, the selectivity can be further enhanced by tuning the lasers according to the optical isotope shift, i.e. small differences in the electronic level energies due to the variations in the structure of the nucleus and its interactions with the electrons. During the sputter process in the TOF-SIMS, only a fraction of the sample material is released as SIs. A lot of material is sputtered as secondary neutrals (SNs) which are usually lost for analysis (Benninghoven et al., 1993). By combining TOF-SIMS and RIMS to resonant laser secondary neutral mass spectrometry (rL-SNMS), these SNs become available for analysis and allow for confirmation that the signal observed is indeed the element in question since it is possible to record the background in rL-SNMS by tuning the lasers off resonance, which is not possible with TOF-SIMS (Bosco et al., 2021; Schönenbach et al., 2021; Raiwa et al., 2022; van Eerten et al., 2023). It is important to note that neither TOF-SIMS nor rL-SNMS can directly quantify an analyte without an externally calibrated standard with the exact same sample matrix as reference. Without such a reference material only qualitative comparisons can be made.

In this work, TOF-SIMS and rL-SNMS were applied for the study of the diffusion of Pu in OPA for the first time. The goal was to showcase and evaluate the capability of the combination of both methods to retrieve the diffusion profile of Pu while at the same time preserving the sample matrix and observing the geochemical interactions of the radionuclide with the various mineral phases present in OPA at the micrometer scale. To achieve this, a new workflow for simple and fast diffusion sample preparation tailored to TOF-SIMS and rL-SNMS was developed. For further insight into the complex redox chemistry behaviour of Pu, its oxidation state in the OPA pore water diffusion reservoir was analyzed using capillary electrophoresis coupled to an inductively coupled plasma mass spectrometer (CE-ICP-MS).

2. Materials and methods

2.1. Sample preparation

Cylindrical samples of aerobic OPA ($\varnothing = 5$ mm, $L \approx 15$ mm) were CNC milled dry from larger chunks of bulk OPA (D25 (L11), Mont Terri Rock Laboratory, St-Ursanne, Switzerland) under atmospheric conditions. All further sample preparations were conducted in a fume hood open to ambient air. The cylinders were embedded into custom PMMA sample holders using a slow curing epoxy resin (EpoxiCure™ 2, Buehler, Lake Bluff, Illinois, USA) with the natural bedding of the OPA perpendicular to the in-diffusion contact surface (compare Fig. 1 a & b) and placed in contact with artificial aerobic OPA pore water (OPA-PW) with an ionic strength of approximately 0.39 mol L^{-1} prepared after Pearson (1998) to re-saturate the material and allow it to swell (for the exact composition compare supporting information Table S1). To note, in this step the samples were not hung in the reservoir with the contact surface facing down, but laid on their long side to avoid air entrapment.

After a minimum contact time of 10 d, the contact surface was wet-sanded flat. The OPA samples were then stored in OPA-PW until use for an experiment. No alterations were observed even after three months. The ^{242}Pu(VI) stock solution was prepared by evaporating a ^{242}Pu

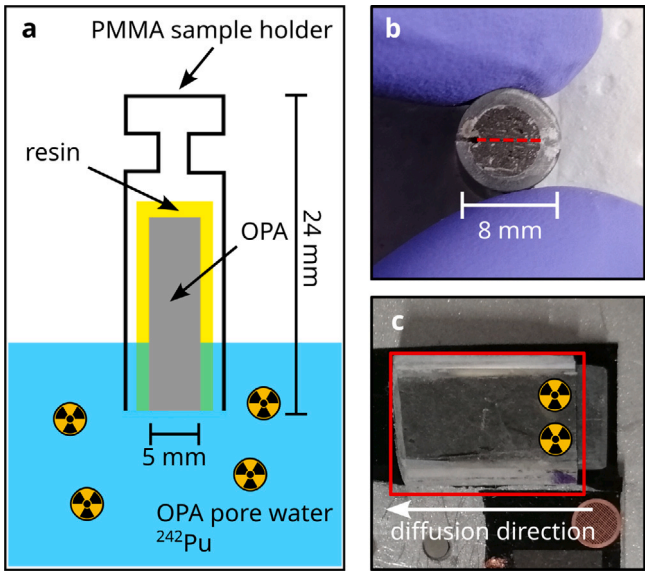

Fig. 1. **a** Schematic of diffusion sample in contact with the pore water solution containing ^{242}Pu. **b** View of the contact surface of a notched diffusion sample. The red line indicates the natural bedding of the OPA along which the sample is then split to allow access to the diffusion profile. **c** Top view of a split diffusion core mounted on a TOF-SIMS sample holder via carbon tape (red square). The Pu diffused into the material from the right edge of the sample and was observed via TOF-SIMS and rL-SNMS.

solution three times with 5 mL of 1 mol L^{-1} $HClO_4$ under heat until near dryness before the residue was picked up in 3 mL of 1 mol L^{-1} $HClO_4$. The Pu oxidation state was then confirmed via UV–VIS (TIDAS 100, J & M Analytik AG, Germany). The concentration of the ^{242}Pu(VI) stock solution ($1.4(8)\times10^{-3}$ mol L^{-1}) was calculated from the absorption band for Pu(VI) at 830 nm using the molar decadic extinction coefficient $\epsilon = 555$ L mol^{-1} cm^{-1} (Clark et al., 2008). An aliquot of the freshly prepared stock solution was then added to 50 mL of OPA-PW (pH 7.7(1), Eh = 650(10) mV (SHE)) to achieve a concentration of 5×10^{-6} mol L^{-1} ^{242}Pu(VI) in a standard laboratory flask (100 mL laboratory bottle, narrow neck, with screw cap, VWR International, Leuven, Belgium). An aliquot of 100 µL of a 1.5 mol L^{-1} NaN_3 solution was added to the reservoir to prevent bacterial or algae growth. The pH was measured using an inoLab© pH 720 meter (WTW© a Xylem brand, Weilheim, Germany) and an SI Analytics™ BlueLine 16 pH micro-electrode (SI Analytics™ a Xylem brand, Mainz, Germany) filled with 3 mol L^{-1} NaCl solution. The pH meter was calibrated using buffer solutions at pH 6.87 (Schott Instruments, L4790) and pH 9.18 (Certipur®, Merck KGaA, Darmstadt, Germany). For Eh measurements a Pt ring electrode with 3 mol L^{-1} KCl (6.0451.100, METROHM Prozessanalytik GmbH & Co. KG, Filderstadt, Germany) was used. The electrode was tested using a redox buffer solution (Eh = 640 mV (SHE), SI Anlytics™ a Xylem brand, Mainz, Germany). The ^{242}Pu concentration in the OPA-PW was monitored via liquid scintillation counting (LSC; HIDEX 300SL, Hidex Oy, Turku, Finland; cocktail: ULTIMA GOLD™ XR, revvity Germany GmbH, Hamburg, Germany) for the duration of the experiment. The reservoir was sampled for LSC measurements in aliquots of 10 µL (until day 17) and 20 µL (until day 35) of the experiment. After an equilibration time of about seven days, when the Pu concentration and pH were constant, five OPA samples were placed into the solution for up to 35 d under aerobic conditions using a custom designed 3D printed insert out of polylactic acid (PLA) (see SI Figure S1). The diffusion cores were taken out of the reservoir after 21, 25, 28 (2 samples) and 35 d, respectively, of which four samples (one for each time interval) were analyzed via TOF-SIMS and rL-SNMS. The samples were directly split by notching the PMMA sample holder parallel to the natural OPA bedding with a saw and applying as little force as possible with a scalpel to split the

OPA core (see Fig. 1 b). This allowed for access to a pristine surface unaltered by saw marks and with relatively low topography which is favourable for both TOF-SIMS and rL-SNMS (see Fig. 1 c). The samples were then dried for a minimum of one day in a glove box under Ar atmosphere before being transferred into the TOF-SIMS instrument.

2.2. TOF-SIMS and rL-SNMS

The TOF-SIMS instrument used in this work is a commercial TOF-SIMS III (iontof GmbH, Münster, Germany) with the controls upgraded to TOF-SIMS V level including a USB-TDC as well as the iontof Surface Lab 6.6 control and analysis software. The custom titanium:sapphire (Ti:sa) laser system consists of three tunable Ti:sa lasers jointly pumped with circa 45 W at 10 kHz by a frequency-doubled neodymium:yttrium aluminum garnet (Nd:yag) laser (DM532-60, Nexlase GmbH, Gröbenzell, Germany). TOF-SIMS and laser system timings were synchronized for rL-SNMS measurements via a frequency generator (modell 577, BNC, San Rafael, USA). The wavelength of the lasers was monitored quasi-simultaneously by a wavemeter equipped with a switch (WS6-200, Highfinesse, Tübingen, Germany). The laser light was transported to the TOF-SIMS via a multi-mode optical fiber and introduced into the analysis chamber via a view port. The setup has been described in more detail in a previous publication (Schönenbach et al., 2021). The samples were attached via carbon tape to a sample holder and transferred into the TOF-SIMS. The vacuum was $<1 \times 10^{-7}$ mbar during measurements. For TOF-SIMS the field of view (FOV) of 500 µm × 500 µm was scanned 50 times with 512^2 px resolution with one PI shot per pixel. For rL-SNMS the same FOV was scanned 20 times with 256^2 px resolution and ten PI shots per pixel. For the first diffusion sample extracted after 21 d, four non-overlapping FOV were recorded, but only one showed sufficient Pu signal to measure rL-SNMS. For the second sample (25 d) five FOVs, for the third sample (28 d) seven FOVs and for the fourth sample after 35 d, six FOVs were analyzed. For the resonant photo-ionization the three step scheme by Grüning et al. (2004) was used. Laser powers were measured (PowerMax© model PM3 with Fieldmate powermeter, Coherent GmbH, Göttingen, Germany) directly after the fiber before the view port of the TOF-SIMS and were usually around 40 mW for the first excitation step (FES), approximately 400 mW for the second excitation step (SES) and 650 mW for the ionizing step (IS).

2.3. CE-ICP-MS

The electrophoresis measurements to determine the oxidation state of Pu in aerobic OPA-PW were conducted using an Agilent 7100 CE (Agilent Technologies Deutschland GmbH, Waldbronn, Germany) coupled to an Agilent 7900 ICP-MS (Agilent Technologies Deutschland GmbH, Waldbronn, Germany). The CE apparatus was coupled to the ICP-MS using a MiraMist CE nebulizer (Burgener Research, Mississauga, Canada) and a Scott-type spray chamber (AHS Analysentechnik, Tübingen, Germany). A fused silica capillary with 50 µm inner diameter and 50 cm length was used (Polymicro Technologies, Phoenix, Arizona, USA). A voltage of 10 kV was applied to the capillary. The setup and measurement procedure have been described in detail in a previous publication (Willberger et al., 2019). To determine the oxidation state, aliquots of the OPA-PW solution with ^{242}Pu were spiked with 2-bromopropane as electroosmotic flow (EOF) marker. In addition, samples of ^{237}Np(V) in OPA-PW (ca. 1×10^{-7} mol L^{-1}) were prepared the same way and analyzed via CE-ICP-MS for comparison. The electrophoretic mobility μ_e was calculated from the retention times of the analyte (t) and the EOF marker (t_{EOF}) as well as the length of the capillary (L) and the applied voltage (U) according to Eq. (1) (Willberger et al., 2019):

$$\mu_e = \frac{L^2}{U} \cdot \left(\frac{1}{t} - \frac{1}{t_{\mathrm{EOF}}} \right), [\mu_e] = \frac{\mathrm{m}^2}{\mathrm{V \cdot s}}. \quad (1)$$

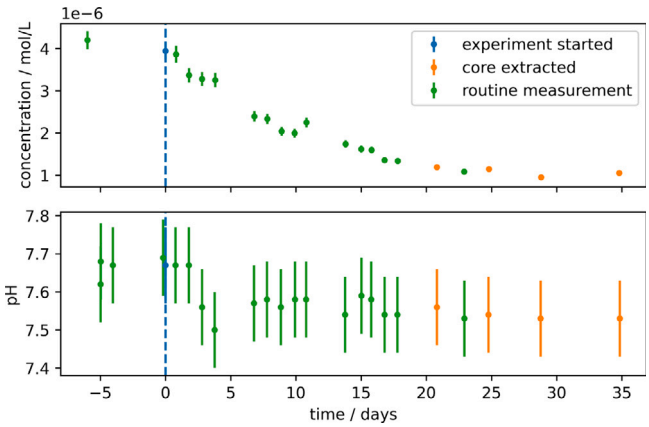

Fig. 2. Concentration of ^{242}Pu monitored by LSC in the reservoir (V = 50 mL) for the duration of the diffusion experiment and the measured pH. To ensure a stable Pu concentration in the reservoir, a measurement was performed before the addition of the diffusion cores and the start of the experiment indicated by the blue dashed line. A reduction of Pu concentration in solution by a factor of 4 is observed 35 d after starting the experiment with most of the decrease happening within 21 d of in-diffusion. The pH of the OPA-PW solution was at around 7.6 for the whole duration of the experiment. Four diffusion samples were analyzed after 21, 25, 28 and 35 days of contact time, respectively, via TOF-SIMS and rL-SNMS.

3. Results and discussion

3.1. Analysis of the OPA-PW diffusion reservoir

As shown in Fig. 2, immediately after inserting the OPA diffusion samples, the ^{242}Pu concentration of the reservoir decreased and stabilized after approximately 21 d, indicating an initial high uptake of Pu by the samples. The pH of the reservoir solution remained nearly constant for the whole duration of the experiment, with only a slight drop of 0.1 pH units 3 d into the experiment.

The trend is comparable to previous diffusion experiments with Np(V) and OPA (Wu et al., 2009; Fröhlich et al., 2013). The Eh of the solution reduced from initially 650(10) mV to 480(20) mV (SHE) after 35 days. Figure 3 displays the Pourbaix diagram for the system presented here, including the two Eh measurements at the beginning (orange) and after the end of the experiment (blue). Since this experiment was conducted under oxidizing conditions, the values are higher than in the reducing conditions in the host rock: Field measurements in different OPA boreholes in Mont Terri resulted in Eh values between −120 mV to 140 mV (SHE) (Pearson et al., 2003).

The theoretical calculation for the diffusion system suggests that in the beginning the majority of Pu was present as $PuO_2^+(aq)$ but with the change of the Eh $Pu(OH)_4(aq)$ should be the dominating species. In order to evaluate the oxidation state of Pu in the reservoir at the end of the experiment, CE-ICP-MS measurements of an aliquot of the reservoir OPA-PW solution were performed. Figure 4 shows the electrophoretic mobility determined via CE-ICP-MS for ^{242}Pu and ^{237}Np in OPA-PW, with the sample for ^{242}Pu taken from the diffusion reservoir used in this study after the experiment had ended. Both isotopes are displaying the same positive μ_e, suggesting that they are present in OPA-PW as similar chemical species, despite having different initial oxidation states (^{242}Pu: VI and ^{237}Np: V) when they were added initially to OPA-PW under aerobic conditions.

Since Np is stable as $NpO_2^+(aq)$ under these conditions, this suggests that Pu is present as $PuO_2^+(aq)$ in the reservoir solution. As mentioned above, the Pourbaix diagram for the system suggests as well that under the initial conditions of the contact solution (pH 7.7(1), Eh = 650(10) mV (SHE)) the majority of Pu should be Pu(V). However, the theoretical calculations would predict Pu(IV) to be the dominating species for the Eh = 480(20) mV measured after finishing the diffusion experiment,

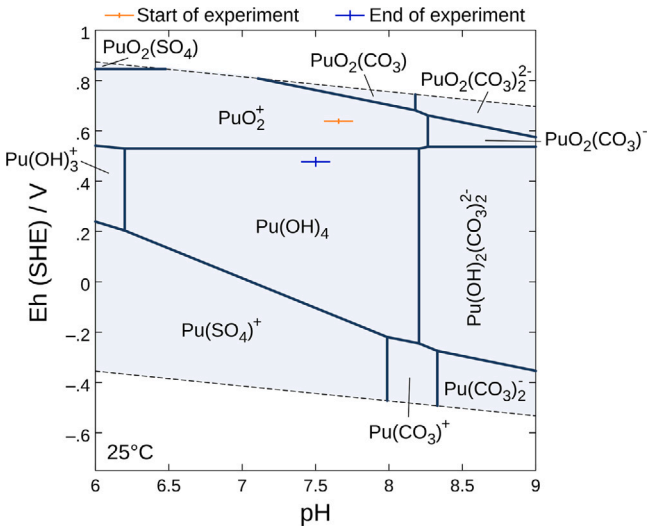

Fig. 3. Pourbaix diagram of 4×10^{-6} mol L^{-1} Pu in OPA-PW under aerobic conditions. Calculated using The Geochemist's Workbench® 2023 Community Edition, Release 17.0.3 and the Thermochimie Database v12a (Giffaut et al., 2014). Composition of OPA-PW according to Pearson (1998) without Sr. A concentration of 420 ppm CO_2 in the atmosphere was assumed. Mineral phases were suppressed since no precipitation was observed during the experiment. The Eh and pH measured in the ^{242}Pu containing OPA-PW contact solution before the start of the experiment (pH 7.7(1), Eh = 650(10) mV (SHE)) and at the end of the experiment (pH 7.6(1), Eh = 480(20) mV (SHE)) after 35 days are shown in orange and blue, respectively.

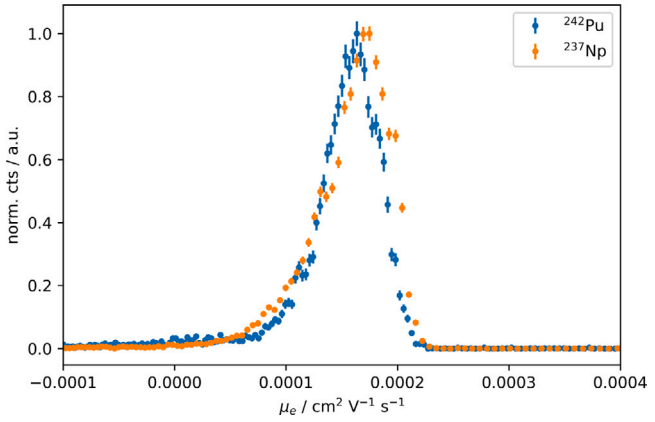

Fig. 4. Comparison of the electrophoretic mobilities (μ_e) of ^{237}Np (initial ox. state V) and ^{242}Pu (initial ox. state VI) in OPA-PW at pH 7.6(1), Eh = 480(20) mV (SHE). Since Pu is displaying the same μ_e as Np(V) which is stable as $NpO_2^+(aq)$ under these conditions, it follows that also Pu exists as $PuO_2^+(aq)$ in the OPA-PW reservoir.

but Pu(IV) was not detected in the CE-ICP-MS measurement. Possible explanations include the decreased solubility of $Pu(OH)_4$ compared to PuO_2^+ for pH 7.6(1) (Neck et al., 2007) below the detection limit of the CE-ICP-MS system or increased sorption of Pu(IV) to the sample or reservoir surfaces since no precipitation was observed either by visual inspection or in the CE-ICP-MS measurements. CE-ICP-MS is sensitive to the presence of colloids or precipitation and no centrifugation of the sample was necessary to obtain an analyte signal free of interferences. Our result suggests that Pu(VI) was reduced to Pu(V) in OPA-PW in the experiment's reservoir under aerobic conditions at pH 7.6 and was present predominantly as PuO_2^+. A recent study by Kaplan et al. (2024) on Pu(V) diffusion in OPA using X-ray absorption fine structure spectroscopy (XAFS) showed that Pu(V) was subsequently reduced to the less mobile oxidation and stronger sorbing state Pu(IV) inside the clay rock with the relative amount of Pu(V) decreasing with increasing

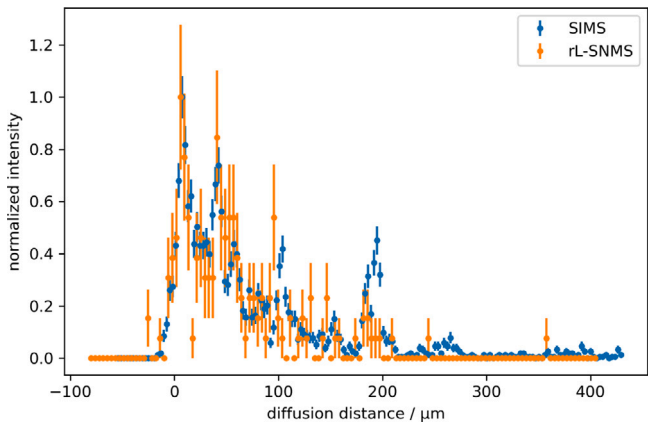

Fig. 5. Diffusion profiles extracted from the distributions of Pu obtained via TOF-SIMS (the sum of $^{242}Pu^+$ and $^{242}PuO^+$) and rL-SNMS (Pu^+) in Fig. 6 for a single FOV with 500 μm × 500 μm. The profiles were obtained by summing up the signal intensity in each row along the direction of the diffusion in the distribution for the respective masses. Both profiles show intensity spikes which are the result of areas with increased intensity in the Pu distributions. The data has been binned with a binning increment of two. Error bars are calculated as $\sigma = \sqrt{N}$ with N the number of events detected.

diffusion depth. At this point, further studies via CE-ICP-MS are necessary to determine the kinetics of the formation of Pu(V) from Pu(VI) and the role of Pu(IV) in the OPA-PW reservoir solution.

3.2. TOF-SIMS and rL-SNMS measurements of the Pu diffusion profile

During analysis, no significant differences between the first three samples removed from the reservoir after 21 d, 24 d and 28 d with regard to diffusion depth and distribution of Pu were observed. Therefore, the discussion is focused on the two samples in contact with Pu for 21 d and 35 d, respectively.

Figure 5 shows the Pu diffusion profiles retrieved via TOF-SIMS and rL-SNMS for a single FOV with 500 μm × 500 μm from the first sample extracted after 21 d of contact time. The profile is generated from the respective distribution image for Pu shown in Fig. 6 by summing the intensity of each row parallel to the sample interface, thereby constructing the profile along the diffusion direction into the sample.

Both TOF-SIMS and rL-SNMS profiles show that more ^{242}Pu is located near the interface of solution and OPA and the overall signal decreases with increasing depth. ^{242}Pu migrated approximately 280 μm into the sample within 21 d, which is comparable to the literature (Kaplan et al., 2024). However, the diffusion profiles include spikes in the signal which have not been reported from comparable experiments using abrasive methods.

Figure 6 displays the total ion image and Ca^+ distribution for a 500 μm × 500 μm area at the interface of the OPA sample and the contact solution indicated by the dashed white line as well the distribution of Pu observed via TOF-SIMS and rL-SNMS from which the profiles in Fig. 5 were generated. The total ion image gives a general idea of the topography and microstructure of the sample. Although the sample was split parallel to its natural bedding, it still displays differences in height, with lower areas showing a reduced signal and therefore topographic interferences of the signal cannot be fully excluded and need to be taken into account. As already established in the description of the profile, both TOF-SIMS and rL-SNMS show a higher abundance of Pu towards the edge of the sample and interface with the OPA-PW indicated by the dashed white line (see Fig. 6) as well as a decrease in signal with increasing diffusion depth. But, similar to Ca^+, Pu has a heterogeneous distribution in contrast to other elements such as Si or K (see SI Figure S2) and shows areas of high intensity or 'hot spots', that cannot be explained by the topography and which are the origin of

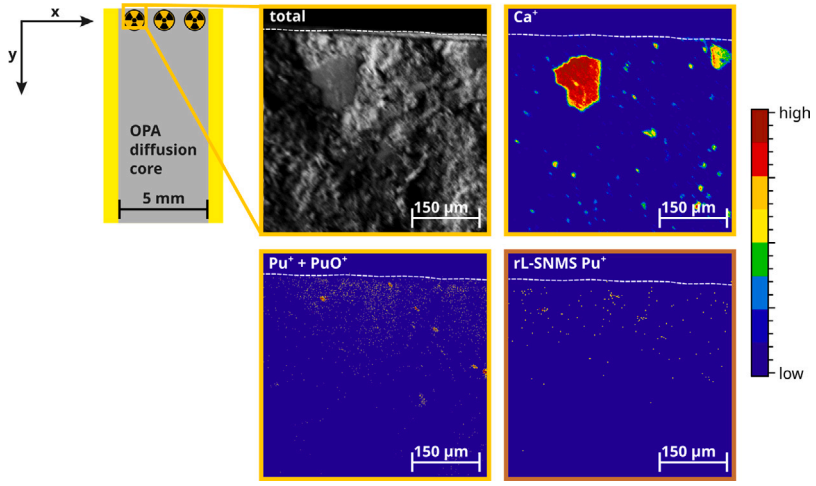

Fig. 6. Total ion image (top left) and Ca^+ (m/z = 40 u, top right), as well as the distributions of Pu^+ plus PuO^+ (m/z = 242 u and 258 u, bottom left) observed via TOF-SIMS compared to Pu^+ detected by rL-SNMS (m/z = 242 u, bottom right) in a 500 µm × 500 µm measured window on an OPA diffusion core in contact after 21 d. The white dashed line indicates the interface of the sample and the ^{242}Pu spiked OPA-PW solution. The direction of diffusion is parallel to the y-axis. TOF-SIMS was measured with 512^2 px resolution, rL-SNMS with 256^2 px. The rL-SNMS signal for Pu is significantly smaller than the sum of Pu^+ and PuO^+ for a comparable measurement time, suggesting the resonant photo-ionization of Pu is less efficient. Nevertheless, a resonant signal is observed. Additional matrix element distributions observed by TOF-SIMS can be found in SI Figure S2.

the deviations from a smooth diffusion profile observed in Fig. 5. Additionally, in some areas of high Ca^+ intensity, that can be attributed to calcite when looking at the microstructure visible in the total ion image, the Pu signal is reduced. In general, both TOF-SIMS and rL-SNMS show the same distribution, but the total ion signal for $^{242}Pu^+$ detected by rL-SNMS is lower compared to TOF-SIMS. First, this can be explained that using TOF-SIMS $^{242}Pu^+$ and $^{242}PuO^+$ can be observed, whereas for rL-SNMS only $^{242}Pu^+$ is detected. Second, with the current laser setup no signal saturation is reached in the IS, resulting in only partial ionization of available ions (Schönenbach et al., 2021). In addition, only Pu sputtered as neutral species is available for being resonantly ionized from the ground state, so a possible explanation would also be that the percentage of sputtered neutrals might be reduced for this type of matrix. Here, further investigations are necessary. However, despite the lower intensity, rL-SNMS allows in its current development state to confirm the distribution retrieved via TOF-SIMS and gives a direct method to attribute the signal for m/z = 242 u to $^{242}Pu^+$.

Figure 7 (top right) shows the Pu distribution observed via TOF-SIMS in a representative FOV for the fourth diffusion sample extracted after 35 d of being in contact with the ^{242}Pu containing reservoir solution.

Also here, the diffusion profile (see SI Figure S4) and the distribution image indicate similar areas of increased ^{242}Pu signal that are not explained by the topography shown in the total ion image. Upon comparison with other elements, a correlation between the Pu^+, PuO^+, Fe^+ and Ca^+ for the 'hot spots' is observed (Fig. 7 bottom). To note, in some areas for Ca^+ an anti-correlation with Pu as discussed for the previous sample (Fig. 6) can also be identified. These observations are also confirmed by scatter plots Fig. 8 of the normalized intensities for Fe^+, Ca^+ and the sum of Pu^+ and PuO^+ for the magnified FOVs shown in Fig. 7, bottom row.

The intensity for the combined Pu signal of Pu^+ and PuO^+ is correlated with Fe^+ (compare Fig. 8 **a**). Also for the intensity of the Ca^+ signal there is a correlation with Pu, but an increased signal of Ca^+ does not lead to an increase in Pu (Fig. 8 **b**). The scatter plot for the signal intensity of Fe^+ and Ca^+ (Fig. 8 **c**) also suggests an influence on the Fe^+ signal by the presence of Ca^+. However, also here a high Ca^+ intensity does not cause a high Fe^+ signal. As mentioned before this confirms the observation of areas with a high Ca^+ intensity in the mapping shown in Fig. 7 that have no co-localization with Pu or Fe.

For the areas with a positive correlation, an isobaric interference between CaO^+ and Fe^+ was excluded by comparing the ratio $^{54}Fe^+/^{56}Fe^+$ for the positions 1–5 (compare Fig. 7 bottom) on the sample's surface that is in excellent agreement with the literature value 0.0637(11) (De Laeter et al., 2003) (see Table 1) for the natural isotopic ratio of $^{54}Fe^+$ and $^{56}Fe^+$.

Table 1
$^{54}Fe^+/^{56}Fe^+$ ratios observed for the 'hot spots' in Fig. 7. The ratio agrees with the literature and therefore it is unlikely that isobaric interferences of CaO^+ are observed on mass 56 u.

Position no.	$^{54}Fe^+/^{56}Fe^+$
1	0.063(5)
2	0.071(17)
3	0.061(11)
4	0.066(12)
5	0.062(9)
De Laeter et al. (2003)	0.0637(11)

At this point of the method development and due to instrumental limitations, it is not possible to identify the mineral phases involved via TOF-SIMS and rL-SNMS. Fe bearing minerals in OPA include for example siderite, illite and pyrite. The mineral pyrite (FeS_2) has already been indicated in literature as one potential mineral phase of OPA that is involved in the retention of radionuclides (Fröhlich et al., 2012; Reich et al., 2016; Kaplan et al., 2017). Pyrite is present in clay rocks as sub-mm-sized aggregates (Greer, 1978; Wang et al., 2013) associated with a cementitious calcite phase (Lerouge et al., 2014; Breckheimer et al., 2023), which could explain the observed correlation with Ca^+. Unfortunately, due to the isobaric interference of O_2^- on mass 32 u and an increased background on non-conducting samples, it was not possible to detect ^{32}S or other isotopes of S in negative ion mode TOF-SIMS. Furthermore, the influence of the so-called matrix effect, i.e. changes in the sputter rate of the different elements due to the chemical surrounding, cannot be excluded. Additional information from other chemical imaging techniques such as μ-XRD or μ-XRF could provide answers in the future. This is also true for the oxidation state of the Fe in the iron bearing mineral. Due to the aerobic nature of the OPA sample and the experiment, at least partial oxidation and therefore changes in the redox behaviour, especially towards the interface of the sample, have to be assumed. Here, XANES and XRD measurements at a synchrotron facility could provide further insights. In general, no differences in the distribution of Pu were observed between the two samples (21 d and 35 d of contact time with Pu, respectively) discussed

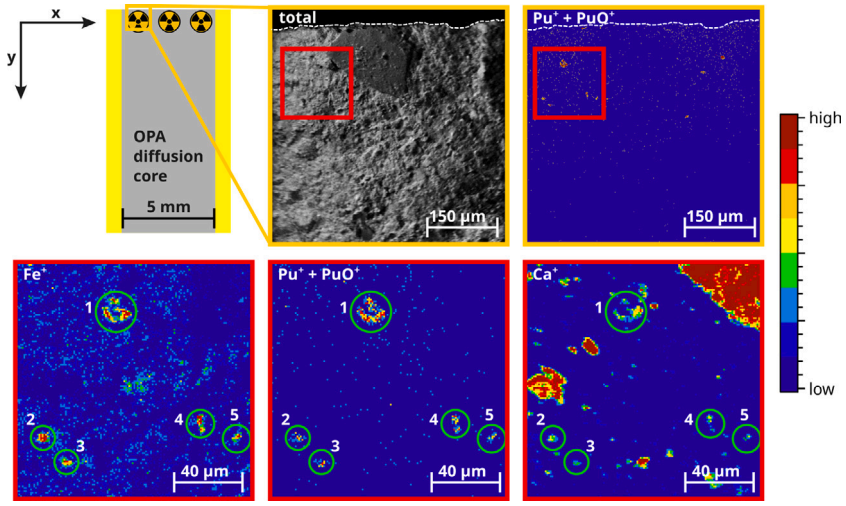

Fig. 7. Total ion image and Pu^+ plus PuO^+ (m/z = 242 u and m/z = 258 u) distributions as observed by TOF-SIMS on an OPA diffusion sample after 35 d (top row). Also in this sample 'hot spots' of Pu are observed. For the area marked by the red square, the distributions of Fe^+ (m/z = 56 u), Pu^+ and PuO^+ as well as Ca^+ (m/z = 40 u) are displayed as magnifications (bottom row). Here, a correlation between all three masses is observed for the Pu 'hot spots'. To rule out an isobaric interference by CaO^+ on the same mass as Fe^+, the areas 1–5 marked by green circles have been analyzed for the $^{54}Fe^+/^{56}Fe^+$ ratio (see Table 1) which is in excellent agreement with the literature value 0.0637(11) (De Laeter et al., 2003). FOV: 500 µm × 500 µm, 512^2 px. Additional matrix element distributions observed by TOF-SIMS can be found in SI Figure S3.

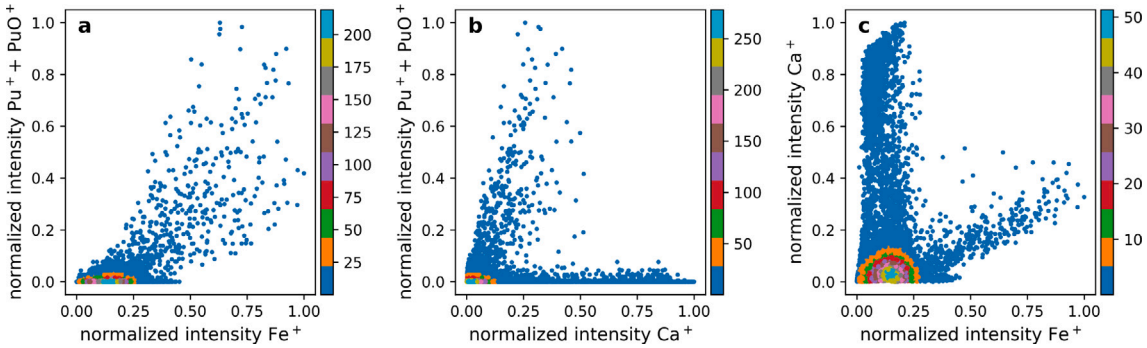

Fig. 8. Normalized intensity scatter plots of $Fe^+/(Pu^+ + PuO^+)$ **(a)**, $Ca^+/(Pu^+ + PuO^+)$ **(b)** and Fe^+/Ca^+ **(c)** for the FOVs displayed in the bottom row of Fig. 7. The intensity scatter plots were generated by applying a Gaussian filter with $\sigma = 1$ to the normalized 140^2 px raw data matrix for the respective mass peaks using custom scripts. The color scale indicates point density and was retrieved via a Gaussian kernel density estimate (Virtanen et al., 2020) of the filtered data matrix.

and only a slight increase of the diffusion depth of around 20 µm and an overall increase of Pu signal intensity was noted. It is also important to mention that since the splitting of the sample is done along the natural bedding, it might separate along a weakened natural potential fracture layer and therefore greater and faster diffusion is observed.

3.3. Modeling of an averaged diffusion profile

Since for the fourth diffusion sample placed in contact with Pu for 35 d six different 500 µm × 500 µm FOVs with sufficient Pu signal were measured via TOF-SIMS, it is possible to average over all six profiles and therefore minimize the influence of the 'hot spots' already discussed. This yields a profile that is comparable to the ones retrieved via classic abrasive peeling. A novel workflow using custom python scripts for the registration of the edges of each profile and averaging was developed. Since TOF-SIMS does not allow for direct quantification of the analyte signal, a dimensionless approach such as the solution of Fick's law shown in Eq. (2) by Yaroshchuk and Van Loon (2008) is required. This allows to use the signal intensity of the TOF-SIMS measurement directly.

$$c(\xi_*, \tau_*) = exp(\xi_* + \tau_*) \cdot erfc\left(\sqrt{\tau_*} + \frac{\xi_*}{2 \cdot \sqrt{\tau_*}}\right). \quad (2)$$

The diffusion normalized diffusion depth ξ is calculated from the diffusion depth x and the length l_* according to Eq. (3) with α the rock capacity factor, the reservoir volume V and the contact surface area of the OPA diffusion core S:

$$\xi_* = x/l_* \text{ with } l_* = \frac{V}{\alpha \cdot S}. \quad (3)$$

The normalized diffusion time τ_* is calculated according to Eq. (4) via the diffusion time t, α, the effective diffusion coefficient D_e, as well as the before mentioned V and S:

$$\tau_* = \frac{t}{t_*} \text{ with } t_* = \frac{1}{\alpha \cdot D_e} \cdot \left(\frac{V}{S}\right)^2. \quad (4)$$

Under the assumption that the maximum counts cts_{max} for Pu observed via TOF-SIMS directly at the interface correlate with the concentration of Pu in the reservoir, the intensity of the TOF-SIMS signal is normalized to cts_{max}. It is important to note that this model does not account for changing concentration in the reservoir and for redox processes inside the sample. An additional assumption required is that the 'rising edge' at the sample interface is an artifact of the TOF-SIMS measurement and not a Pu wavefront moving into the sample. This is the prerequisite for excluding these data points from the fit since the model cannot account for such a shape. For this reason it needs to be stressed that the diffusion coefficient D_e and the rock capacity factor α retrieved from the fit are only a rough approximation but nevertheless an important showcase for the potential to model a diffusion profile observed via TOF-SIMS. Further work and more advanced diffusion models are necessary to reach the full potential of the data. The fit was

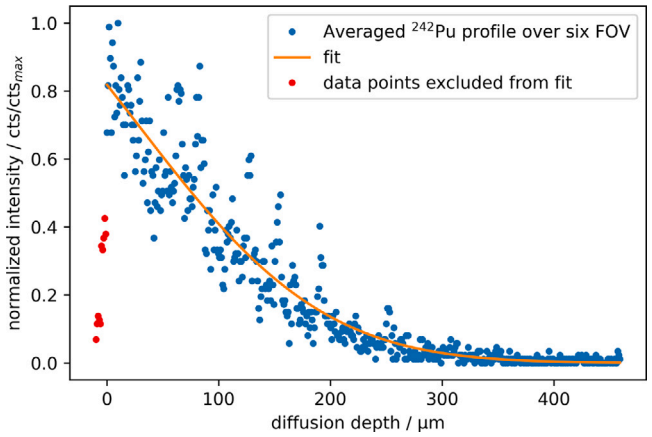

Fig. 9. Fit of the averaged Pu diffusion profile for the fourth diffusion sample (35 d). A total of six separate 500 µm × 500 µm FOV were measured via TOF-SIMS along the interface of the OPA diffusion core. The obtained profiles were aligned and averaged.

Table 2
Constants and fit parameters retrieved for the fit of an Pu diffusion profile obtained by averaging over six FOVs measured by TOF-SIMS (Fig. 9) using the model in Eq. (2).

Parameter	Value
V / m^3	5×10^{-5}
S / m^2	1.96×10^{-5}
t / s	3 024 000
D_e / m^2 s^{-1}	$1.6(2) \times 10^{-11}$
α / –	4853(358)
D_a / m^2 s^{-1}	$3.2(4) \times 10^{-15}$

performed using custom python scripts and the lmfit package (Newville et al., 2024). Figure 9 shows the averaged diffusion profile and the fit to Eq. (2). The individual profiles for each of the six FOVs averaged are shown in the SI Figure S5.

Despite the already discussed restrictions of the model, it is able to reproduce the data. The main difficulty is to locate the beginning of the profile since the fit does not start at the highest intensity at the beginning of the profile. In addition, spikes in signal intensity originating from intensity spikes in the individual profiles are still visible, but their significance is reduced. The used constants and retrieved diffusion parameters are listed in Table 2. The apparent diffusion coefficient D_a was calculated from D_e/α.

The model results in $D_e = 1.6(2) \times 10^{-11}$ m^2 s^{-1} and a capacity factor of $\alpha = 4853(358)$ for this dataset. Using Eq. (5) (Yaroshchuk and Van Loon, 2008) and typical literature values for the porosity ϵ (0.15(1) Wu et al., 2009; Joseph et al., 2013) and density ρ (≈2400 kg m^{-3} Wu et al., 2009; Joseph et al., 2013) of OPA, a theoretical distribution coefficient R_d of approximately 2.4 m^3 kg^{-1} for Pu in OPA can be calculated.

$$\alpha = \epsilon + (1 - \epsilon) \cdot \rho \cdot R_d. \quad (5)$$

However, these values have only a very limited significance due to the strong correlation of α and D_e (C(α, D_e) = 0.94). The apparent diffusion coefficient D_a is a more reliable parameter, since already small changes to the dataset, e.g. binning, influence D_e and α, but their ratio D_a is constant within the margin of error (compare SI Figure S6 and Table S2). When compared to literature, the retrieved D_a(Pu) = $3.2(4) \times 10^{-15}$ m^2 s^{-1} is smaller in relation to experiments with other actinides, such as U(VI) (D_a(U(VI)) = $3.1(3) \times 10^{-14}$ m^2 s^{-1} Joseph et al., 2013) or Np(V) (D_a(Np(V)) = $2.8(5) \times 10^{-14}$ m^2 s^{-1}, calculated from Wu et al., 2009). This suggests that under the settings of the experiment conducted, Pu diffuses slower in OPA than other minor actinides.

4. Conclusions

TOF-SIMS and rL-SNMS were successfully applied to study the diffusion of 4×10^{-6} mol L^{-1} Pu(V) in Opalinus Clay with clay pore water as mobile phase under ambient air conditions. For the in-diffusion experiments a novel, easily scalable setup with small clay cylinders ($\varnothing$ = 5 mm, L ≈15 mm) was developed using modern 3D printing techniques. The in-diffusion experiments lasted up to 35 d. At the end of the diffusion experiment, the electrophoretic mobility of Pu in the sample reservoir was determined by CE-ICP-MS and compared to Np(V). This measurement showed that PuO_2^+ is the main species in the aqueous phase of the diffusion reservoir at pH 7.6 under ambient air conditions.

By cleaving the clay cylinders parallel to the natural bedding of the clay, several 500 µm × 500 µm areas (FOVs) of the pristine clay surface were investigated at the micrometer scale using TOF-SIMS and rL-SNMS. By measuring multiple FOVs along the interface of the OPA core and the reservoir, it was possible to retrieve an averaged diffusion profile of Pu comparable with the classic abrasive peeling technique used for strongly sorbing radionuclides (Van Loon and Müller, 2014). The determined apparent diffusion coefficient $D_a = 3.2(4) \times 10^{-15}$ m^2 s^{-1} of Pu is smaller compared to values found in literature for the diffusion of U(VI) and Np(V) in OPA, suggesting that Pu is less mobile. However, due to limitations of the diffusion model, this is subject of further investigations, which should also consider the complex redox chemistry of Pu in the system.

Certain patterns of the reactive transport of Pu inside OPA could be observed by the elemental distributions of Pu and several matrix elements, i.e., Fe and Ca, at the micrometer scale. Scatter plots of the Pu, Fe and Ca signal intensities reveal correlations between areas of increased Pu signal and Fe and Ca. Although the associated mineral phase could not be identified by TOF-SIMS, a comparison with literature (Kaplan et al., 2024, 2017; Breckheimer et al., 2023) points towards the Fe(II) bearing mineral pyrite with a cementing phase of calcite as the cause for Pu 'hot spots'. The presence of Pu could be confirmed by rL-SNMS, despite its signal for Pu in OPA was significantly reduced compared to the TOF-SIMS signal for Pu^+ and PuO^+. Possible reasons for this include an insufficient sputter rate of atomic Pu necessary for resonant photoionization in the chemical matrix of OPA or insufficient laser power for saturating the ionizing step. The latter is currently being addressed with the setup of a new laser system that allows for higher laser powers and the application of novel excitation schemes for actinides (Savina et al., 2018; Kneip et al., 2020; Kaja et al., 2024). In future investigations of diffusion samples with several actinides present solution, rL-SNMS will be used to resolve isobaric interferences, e.g., between $^{238}UH^+$ and $^{239}Pu^+$.

In conclusion, the combined approach of TOF-SIMS and rL-SNMS allows for faster access to diffusion profiles of strongly sorbing radionuclides compared to the classic abrasive peeling technique while retaining detailed chemical information at the micrometer scale. In the context of the safety assessment for the long-term storage of nuclear waste, both methods are powerful tools for the analysis of transport processes in porous media like argillaceous rocks or concrete. This will facilitate future diffusion experiments with other radionuclides, longer diffusion times and other chemical conditions, e.g. in the presence of organic substances like cement additives or waste constituents (Tasi et al., 2021).

CRediT authorship contribution statement

Felix Berg: Writing – review & editing, Writing – original draft, Visualization, Project administration, Methodology, Investigation, Formal analysis, Conceptualization. **Christopher Sirleaf:** Writing – review & editing, Investigation. **Janik Lohmann:** Writing – review & editing, Investigation. **Markus Breckheimer:** Writing – review & editing, Methodology, Investigation, Conceptualization. **Tobias Reich:** Writing – review & editing, Supervision, Resources, Project administration, Methodology, Funding acquisition, Conceptualization.

Funding

This project was funded by the Federal Ministry of Education and Research (BMBF) under contract no. 02NUK075B (project SOLARIS). M. B. acknowledges funding from the European Union's Horizon 2020 project EURAD (WP FUTuRE), EC Grant agreement no. 847593.

Declaration of competing interest

The authors declare that they have no known competing financial interests or personal relationships that could have appeared to influence the work reported in this paper.

Acknowledgments

The authors would like to thank Dr. Samer Amayri for his contributions during fruitful discussions, Dr. Daniel Grolimund for providing the Opalinus Clay rock and the mechanical workshops of the Department of Chemistry and the research reactor TRIGA at the Johannes Gutenberg-Universität Mainz for the CNC milling of the samples and production of PMMA sample holders. Furthermore, we would like to thank R. Dagnelie and the second anonymous reviewer for their efforts and helpful comments.

Appendix A. Supplementary data

Supplementary material related to this article can be found online at https://doi.org/10.1016/j.apgeochem.2025.106332.

Data availability

Data will be made available on request.

References

Andra, 2022. Demande d'autorisation de création (DAC). URL https://www.andra.fr/cigeo/les-documents-de-reference#section-14367. (Accessed on Feb. 10th 2025).

Benninghoven, A., Hagenhoff, B., Niehuis, E., 1993. Surface MS: probing real-world samples. Anal. Chem. 65 (14), 630A–640A.

Bosco, H., Hamann, L., Kneip, N., Raiwa, M., Weiss, M., Wendt, K., Walther, C., 2021. New horizons in microparticle forensics: Actinide imaging and detection of ^{238}Pu and ^{242m}Am in hot particles. Sci. Adv. 7 (44), eabj1175.

Breckheimer, M., Amayri, S., Ferreira Sanchez, D., Grolimund, D., Reich, T., 2023. Chemical tomography of pyrite composites extracted from Opalinus Clay and reacted with neptunium and plutonium. In: Book of abstracts, 18th International Conference on Chemistry and Migration Behaviour of Actinides and Fission Products in the Geosphere - Migration. p. 340.

Bundesgesetzblatt, 2017. Repository Site Selection Act (Standortauswahlgesetz - StandAG). Bundesgesetzblatt (26), 1074–1102, URL http://www.bgbl.de/xaver/bgbl/start.xav?startbk=Bundesanzeiger_BGBl&jumpTo=bgbl117s1074.pdf.

Churakov, S.V., Hummel, W., Fernandes, M.M., 2020. Fundamental research on radiochemistry of geological nuclear waste disposal. Chimia 74 (12), 1000.

Clark, D.L., Hecker, S.S., Jarvinen, G.D., Neu, M.P., 2008. Plutonium, In: Morss, L.R., Edelstein, N.M., Fuger, J. (Eds.), third ed. In: The Chemistry of the Actinide and Transactinde Elements, vol. 2, Springer, pp. 813–1264 (Chapter 7).

De Laeter, J.R., Böhlke, J.K., De Bievre, P., Hidaka, H., Peiser, H., Rosman, K., Taylor, P., 2003. Atomic weights of the elements. Review 2000 (IUPAC Technical Report). Pure Appl. Chem. 75 (6), 683–800.

Fröhlich, D., Amayri, S., Drebert, J., Grolimund, D., Huth, J., Kaplan, U., Krause, J., Reich, T., 2012. Speciation of Np(V) uptake by Opalinus Clay using synchrotron microbeam techniques. Anal. Bioanal. Chem. 404, 2151–2162.

Fröhlich, D., Amayri, S., Drebert, J., Reich, T., 2013. Influence of humic acid on neptunium(V) sorption and diffusion in Opalinus Clay. Radiochim. Acta 101 (9), 553–560.

Geckeis, H., Zavarin, M., Salbu, B., Lind, O.C., Skipperud, L., 2019. Environmental chemistry of plutonium, second ed. In: Plutonium Handbook, vol. 4, American Nuclear Society, p. 1979,

Giffaut, E., Grivé, M., Blanc, P., Vieillard, P., Colàs, E., Gailhanou, H., Gaboreau, S., Marty, N., Made, B.t., Duro, L., 2014. Andra thermodynamic database for performance assessment: ThermoChimie. Appl. Geochem. 49, 225–236.

Greer, R.T., 1978. Evaluation of pyrite particle size, shape, and distribution factors. Energy Sources 4 (1), 23–51.

Grüning, C., Huber, G., Klopp, P., Kratz, J., Kunz, P., Passler, G., Trautmann, N., Waldek, A., Wendt, K., 2004. Resonance ionization mass spectrometry for ultratrace analysis of plutonium with a new solid state laser system. Int. J. Mass Spectrom. 235 (2), 171–178.

Joseph, C., Van Loon, L., Jakob, A., Steudtner, R., Schmeide, K., Sachs, S., Bernhard, G., 2013. Diffusion of U(VI) in Opalinus Clay: Influence of temperature and humic acid. Geochim. Cosmochim. Acta 109, 74–89.

Kaja, M., Studer, D., Berg, F., Berndt, S., Düllmann, C.E., Kneip, N., Reich, T., Urquiza-González, M., Wendt, K., 2024. Resonant laser ionization of neptunium: investigation on excitation schemes and the first ionization potential. Eur. Phys. J. D 78 (5), 1–9.

Kaplan, U., Amayri, S., Drebert, J., Grolimund, D., Reich, T., 2024. Plutonium mobility and reactivity in a heterogeneous clay rock barrier accented by synchrotron-based microscopic chemical imaging. Sci. Rep. 14 (1), 1–11.

Kaplan, U., Amayri, S., Drebert, J., Rossberg, A., Grolimund, D., Reich, T., 2017. Geochemical interactions of plutonium with Opalinus Clay studied by spatially resolved synchrotron radiation techniques. Environ. Sci. Technol. 51 (14), 7892–7902.

Kneip, N., Düllmann, C.E., Gadelshin, V., Heinke, R., Mokry, C., Raeder, S., Runke, J., Studer, D., Trautmann, N., Weber, F., Wendt, K., 2020. Highly selective two-step laser ionization schemes for the analysis of actinide mixtures. Hyperfine Interactions 241 (1), 1–7.

Lerouge, C., Grangeon, S., Claret, F., Gaucher, E., Blanc, P., Guerrot, C., Flehoc, C., Wille, G., Mazurek, M., 2014. Mineralogical and isotopic record of diagenesis from the Opalinus Clay formation at Benken, Switzerland: implications for the modeling of pore-water chemistry in a clay formation. Clays Clay Miner. 62 (4), 286–312.

Maes, N., Churakov, S., Glaus, M., Baeyens, B., Dähn, R., Grangeon, S., Charlet, L., Brandt, F., Poonoosamy, J., Hoving, A., et al., 2024. EURAD state-of-the-art report on the understanding of radionuclide retention and transport in clay and crystalline rocks. Front. Nucl. Eng. 3, 1417827.

Montavon, G., Ribet, S., Loni, Y.H., Maia, F., Bailly, C., David, K., Lerouge, C., Madé, B., Robinet, J., Grambow, B., 2022. Uranium retention in a Callovo-Oxfordian clay rock formation: From laboratory-based models to in natura conditions. Chemosphere 299, 134307.

Nagra, 2022. The Site for the Deep Geological Repository - Nagra's Proposal. Tech. Rep., URL https://nagra.ch/wp-content/uploads/2022/09/Report-the-site-for-the-deep-geological-repository-Nagras-proposal.pdf.

Neck, V., Altmaier, M., Seibert, A., Yun, J.-I., Marquardt, C.M., Fanghänel, T., 2007. Solubility and redox reactions of Pu(IV) hydrous oxide: Evidence for the formation of PuO_{2+x}(s, hyd). Radiochim. Acta 95 (4), 193–207.

Newville, M., Otten, R., Nelson, A., Stensitzki, T., Ingargiola, A., Allan, D., Fox, A., Carter, F., Michał, Osborn, R., Pustakhod, D., Weigand, S., lneuhaus, Aristov, A., Glenn, Mark, mgunyho, Deil, C., Hansen, A.L.R., Pasquevich, G., Foks, L., Zobrist, N., Frost, O., Stuermer, Jaskula, J.-C., Caldwell, S., Eendebak, P., Pompili, M., Nielsen, J.H., Persaud, A., 2024. lmfit/lmfit-py: 1.3.2. Zenodo.

Pearson, F., 1998. Opalinus Clay Experimental Water: A1 Type, Version 980318. Tech. Rep. TM-44-98-07, Paul Scherrer Institut, Villigen PSI.

Pearson, F., Arcos, D., Bath, A., Boisson, J., Fernández, A., Gäbler, H., Gaucher, E., Gautschi, A., Griffault, L., Hernán, P., et al., 2003. Mont Terri project-Geochemistry of water in the Opalinus clay formation at the Mont Terri Rock Laboratory. Berichte des BWG, Ser. Geol. 5.

Preter, P.D. (Ed.), 2023. Activity Report 2021 & 2022. EIG EURIDICE, Tech. Rep. EURIDICE/54165858. URL https://www.euridice.be/sites/default/files/editor/Euridice%20Activity%20Report%202021_2022.pdf.

Raiwa, M., Büchner, S., Kneip, N., Weiß, M., Hanemann, P., Fraatz, P., Heller, M., Bosco, H., Weber, F., Wendt, K., Walther, C., 2022. Actinide imaging in environmental hot particles from Chernobyl by rapid spatially resolved resonant laser secondary neutral mass spectrometry. Spectrochim. Acta Part B: At. Spectrosc. 190, 106377.

Reich, T., Amayri, S., Boerner, P.J.B., Drebert, J., Fröhlich, D.R., Grolimund, D., Kaplan, U., 2016. Speciation of neptunium during sorption and diffusion in natural clay. J. Physics: Conf. Ser. 712 (1), 012081.

Savina, M.R., Trappitsch, R., Kucher, A., Isselhardt, B.H., 2018. New resonance ionization mass spectrometry scheme for improved uranium analysis. Anal. Chem. 90 (17), 10551–10558.

Schönenbach, D., Berg, F., Breckheimer, M., Hagenlocher, D., Schönberg, P., Haas, R., Amayri, S., Reich, T., 2021. Development, characterization, and first application of a resonant laser secondary neutral mass spectrometry setup for the research of plutonium in the context of long-term nuclear waste storage. Anal. Bioanal. Chem. 413 (15), 3987–3997.

Tasi, A., Gaona, X., Rabung, T., Fellhauer, D., Rothe, J., Dardenne, K., Lützenkirchen, J., Grive, M., Colas, E., Bruno, J., 2021. Plutonium retention in the isosaccharinate–cement system. Appl. Geochem. 126, 104862.

van Eerten, D., Raiwa, M., Hanemann, P., Leifermann, L., Weissenborn, T., Schulz, W., Weiß, M., Shulaker, D.Z., Boone, P., Willingham, D., Thomas, K., Sammis, B., Isselhardt, B., Savina, M., Walther, C., 2023. Multi-element isotopic analysis of hot particles from Chornobyl. J. Hazard. Mater. 452, 131338.

Van Loon, L.R., Müller, W., 2014. A modified version of the combined in-diffusion/abrasive peeling technique for measuring diffusion of strongly sorbing radionuclides in argillaceous rocks: A test study on the diffusion of caesium in Opalinus Clay. Appl. Radiat. Isot. 90, 197–202.

Virtanen, P., Gommers, R., Oliphant, T.E., Haberland, M., Reddy, T., Cournapeau, D., Burovski, E., Peterson, P., Weckesser, W., Bright, J., van der Walt, S.J., Brett, M., Wilson, J., Millman, K.J., Mayorov, N., Nelson, A.R.J., Jones, E., Kern, R., Larson, E., Carey, C.J., Polat, I., Feng, Y., Moore, E.W., VanderPlas, J., Laxalde, D., Perktold, J., Cimrman, R., Henriksen, I., Quintero, E.A., Harris, C.R., Archibald, A.M., Ribeiro, A.H., Pedregosa, F., van Mulbregt, P., SciPy 1.0 Contributors, 2020. SciPy 1.0: fundamental algorithms for scientific computing in Python. Nature Methods 17 (3), 261–272.

Wang, P., Huang, Y., Wang, C., Feng, Z., Huang, Q., 2013. Pyrite morphology in the first member of the Late Cretaceous Qingshankou formation, Songliao Basin, northeast China. Palaeogeogr. Palaeoclimatol. Palaeoecol. 385, 125–136.

Willberger, C., Amayri, S., Häußler, V., Scholze, R., Reich, T., 2019. Investigation of the electrophoretic mobility of the actinides Th, U, Np, Pu, and Am in different oxidation states. Anal. Chem. 91 (18), 11537–11543.

Wu, T., Amayri, S., Drebert, J., van Loon, L.R., Reich, T., 2009. Neptunium(V) sorption and diffusion in Opalinus Clay. Environ. Sci. Technol. 43 (17), 6567–6571.

Yaroshchuk, A.E., Van Loon, L.R., 2008. Improved interpretation of in-diffusion measurements with confined swelling clays. J. Contam. Hydrol. 97 (1–2), 67–74.